

Incubation and aging effect on cassiterite type tetragonal rutile SnO₂ nanocrystals

Rathinam Yuvakkumar · Sun Ig Hong

Received: 7 December 2014 / Accepted: 10 January 2015 / Published online: 23 January 2015
© Springer Science+Business Media New York 2015

Abstract The effect of incubation and aging on cassiterite type tetragonal rutile SnO₂ nanocrystals employing green synthesis technique has been investigated. The incubation and aging affected the compositional and morphological properties of SnO₂ and not influenced the structural properties of nanocrystals. The incubation and aging further influenced the particle shape and size of the obtained product. XRD results of the obtained product unambiguously revealed the cassiterite type tetragonal rutile phase of SnO₂ nanocrystals. The characteristic Raman peaks observed at 249, 476, 631 and 773 cm⁻¹ were respectively revealed infrared active (E_u), Raman active (E_g), (A_{1g}) and (B_{2g}) vibration modes of pure tetragonal rutile SnO₂ structure. 3d_{3/2} and 3d_{5/2} of XPS peaks observed at 496 and 487 eV was clearly revealed the Sn⁴⁺ state in tetragonal rutile structure. The obtained TEM micrographs clearly revealed that the grain size and agglomeration was increased at higher incubation and aging treatments.

1 Introduction

Inorganic tin dioxide (SnO₂) is the most important material widely used in electronic [1–12] and gas sensing [13–18] applications. For example, Agrahari et al. [19] investigated optoelectronic properties of SnO₂ nanoparticles. Glot et al. [20] explored electrical properties of SnO₂ ceramics for low voltage varistors. Gajendiran et al. [21] studied nano structured aggregated tin oxides (SnO₂/SnO) and their

structural and photoluminescence properties employing hydrothermal method. Han et al. [22] revealed first principles study of magnetic properties of stoichiometric and O deficient low index surfaces of rutile SnO₂. Yang et al. [23] explored the preparation and characterization of p-type transparent conducting SnO thin films. Xu et al. [24] investigated NH₃ gas sensing performance based on electrospun alkaline earth metals composited SnO₂ nanofibers. Reddy et al. [25] revealed low temperature molten salt preparation of nano SnO₂ as anode for lithium-ion batteries. Tao et al. [26] investigated a new way for synthesizing SnO₂ nanosheets. Andersen et al. [27] studied tin dioxide as an effective antioxidant for proton exchange membrane fuel cells. Chen et al. [28] investigated low temperature synthesis of tin dioxide hollow nanospheres and their potential applications in dye sensitized solar cells and photo electrochemical type self powered ultraviolet photo detectors.

In general, the preparation of SnO₂ nanostructure involves minimum neither two precursors nor high temperature, high cost and template assisted synthesis [19–28]. In recent years, mild and sustainable biosynthesis of nanostructures using green protocols has been studied extensively. However, the reports on biosynthesis of SnO₂ nanostructures are scanty. For example, Vidhu et al. [29] studied biogenic synthesis of SnO₂ nanoparticles and its evaluation of antibacterial and antioxidant activities. Srivastava et al. [30] employed biosynthesis of SnO₂ nanoparticles using bacterium *erwinia herbicola* and their photo catalytic activity for degradation of dyes. In the present work, SnO₂ nanocrystals were prepared employing rambutan (*Nephelium lappaceum* L.) peel extract mediated green synthesis route without surfactant and template at room temperature incubation and aging over a period of 1, 4 and 7 days. The prepared nanocrystals were characterized employing standard characterization techniques.

R. Yuvakkumar · S. I. Hong (✉)
Department of Nanomaterials Engineering, Chungnam National University, Daejeon 305-764, South Korea
e-mail: sihong@cnu.ac.kr

2 Experimental sections

2.1 Synthesis of SnO₂ nanocrystals

Initially, 0.1 M aqueous solution of tin (IV) chloride pentahydrate [SnCl₄ · 5H₂O] was prepared. Then, 10 ml rambutan peel extract was added to 50 ml of 0.1 M [SnCl₄ · 5H₂O]. The detailed synthesis procedure was given in our earlier reports [31–34]. The product was stirred about 80 °C for 2 h. The obtained product was then centrifuged; air dried and powdered using mortar and pestle. This powdered sample was calcinated in a muffle furnace at 450 °C for 1 h to get pure SnO₂ nanocrystals.

2.2 Characterization of SnO₂ nanocrystals

The phase and crystalline nature were identified employing X-ray powder diffraction patterns (Bruker AXS, Germany) using CuK α as radiation (1.5406 Å) source. High resolution (Dispersive Raman microscope, Horiba Jobin–Yvon; LabRAM HR UV/vis/NIR) Raman spectroscopy (excitation, 514 nm) was used to confirm SnO₂. Photoluminescence (PL) spectrum was measured (under excitation by 325 nm) with a SPEX double monochromator equipped with L–N₂ cooled Ge detector. Infrared (IR) spectra were recorded employing a Fourier transform infrared spectrophotometer using a Nicolet 520P FT-IR spectrometer. X-ray photoelectron spectra (XPS) were obtained using a MultiLab 2000 spectrometer (Thermo Electron Corporation, UK). Transmission electron microscopic images were obtained using a transmission electron microscope (CM 200; Philips, USA).

3 Results and discussion

The technique for the formation mechanism of metal oxide nanostructures was already discussed in our previous studies [31–34]. The same technique was employed successfully to synthesize SnO₂ nanocrystals in the present study. The structure, phase and morphological variations of SnO₂ nanocrystals incubated at room temperature over a period of 1, 4 and 7 days aging was described in the present study. The XRD pattern of 450 °C calcinated reaction product from the mixture of 0.1 M SnCl₄ · 5H₂O and 10 ml extract incubated with 1, 4 and 7 days of final product are shown in Fig. 1a–c. The obtained product unambiguously revealed the cassiterite type tetragonal rutile phase of SnO₂ nanocrystals. The diffraction peaks (110), (101), (200), (211), (220), (002), (310), (112), (301), (202), (321), (222) and (321) were clearly detected in XRD pattern of the incubated samples which closely matched with expected cassiterite type tin dioxide nanocrystals (JCPDF card file

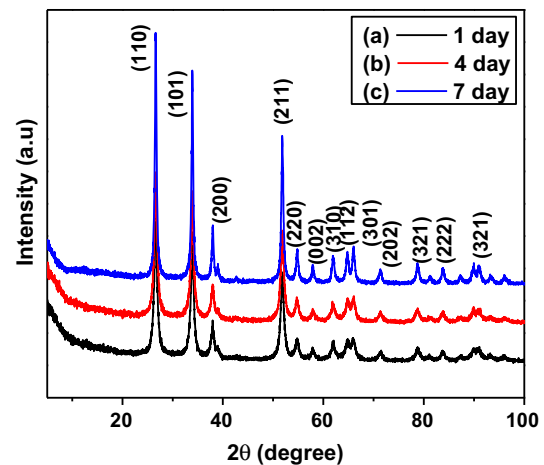


Fig. 1 XRD pattern: reaction product from the mixture of 0.1 M SnCl₄ · 5H₂O and 10 ml extract (a) 1, (b) 4, (c) 7 days

01-072-1147 (A)) with lattice constant $a = 4.73700$, $b = 4.73700$, $c = 3.18500$ Å and $\alpha = 90$, $\beta = 90$, $\gamma = 90$. Rutile has tetragonal D_{4h}^{14} symmetry. All the prominent peaks in the pattern of polycrystalline SnO₂ were indexed on the basis of JCPDF card file 01-072-1147 (A). No other SnO₂ phases was observed and hence revealed high purity of the product [JCPDF card 01-072-1147 (A)]. The relative intensities of the peaks increased over a period of incubation period. The average crystallite size of the prepared tin oxide nanocrystals was calculated using the X-ray diffraction pattern employing the Debye Scherrer formula $D = k\lambda/(\beta\cos\theta)$, where λ is the wavelength of the X-ray radiation, k is a constant taken as 0.898, θ is the diffraction angle and β is the full width at half maximum [31]. The average size of the SnO₂ nanocrystallites deduced from Sherrer's formula for the strongest peak (101) was about 48.7 nm which was nearly consistent with the results observed from the TEM images. Over a period of incubation, diffraction peaks full width half maxima (FWHM) decreased with increased aging period and produced increased average crystallite size. It can be clearly revealed that the peaks were broadened at 1 day incubated product when compared to higher period of incubation.

In addition, the structural and electronic properties of 1, 4 and 7 days incubated product were examined employing Raman spectroscopy. Figure 2a–c shows the Raman spectra of SnO₂ nanocrystals incubated at 1, 4 and 7 days respectively. In general, the expected normal lattice vibrations at Brillouin zone gamma point are $\Gamma = 1A_{1g} + 1A_{2g} + 1A_{2u} + 1B_{1g} + 1B_{2g} + 2B_{1u} + 1E_g + 3E_u$ according to P42/mnm space group. The characteristic Raman peaks observed at 249, 476, 631 and 773 cm⁻¹ were respectively revealed infrared (IR) active (E_u), Raman active (E_g), (A_{1g}) and (B_{2g}) vibration modes of pure tetragonal rutile SnO₂

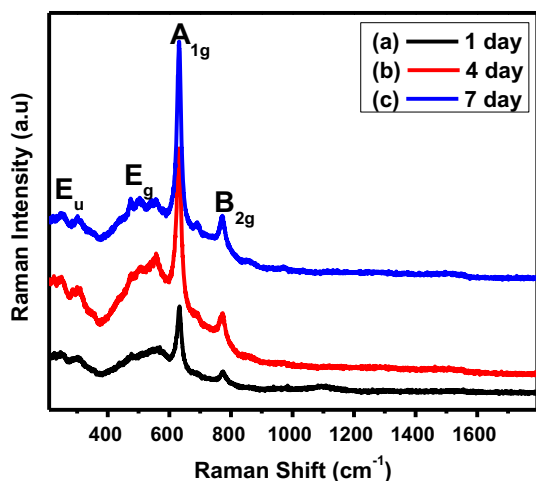


Fig. 2 Raman spectra: reaction product from the mixture of 0.1 M SnCl₄ · 5H₂O and 10 ml extract (a) 1, (b) 4, (c) 7 days

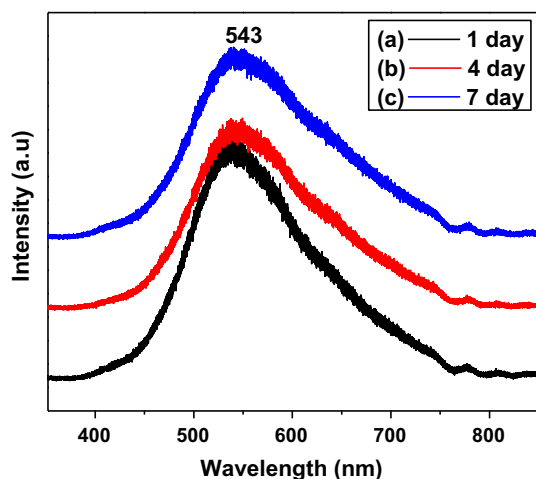


Fig. 3 PL spectra: reaction product from the mixture of 0.1 M SnCl₄ · 5H₂O and 10 ml extract (a) 1, (b) 4, (c) 7 days

structure. Stable rutile phase formation was clearly evidenced in 7 days of incubation treatment. The overall observation from XRD and Raman results confirmed cassiterite type tetragonal rutile structure SnO₂ characteristics.

To explore the defect states of SnO₂ nanocrystals in detail, photoluminescence measurements were carried out at room temperature. Room temperature PL spectra of 1, 4 and 7 days of reaction product mixture are shown in Fig. 3a–c at an excitation wavelength of 325 nm. The obtained nanostructured SnO₂ PL spectra clearly exhibited a strong PL emission in the visible region from 400 to 600 nm ascribed to surface defects related to oxygen vacancies in the near surface region. The obtained nanostructures revealed high degree of crystallinity and broad PL emission peaked in the green emission range 520–540 nm in the visible emission. Due to SnO₂ wide

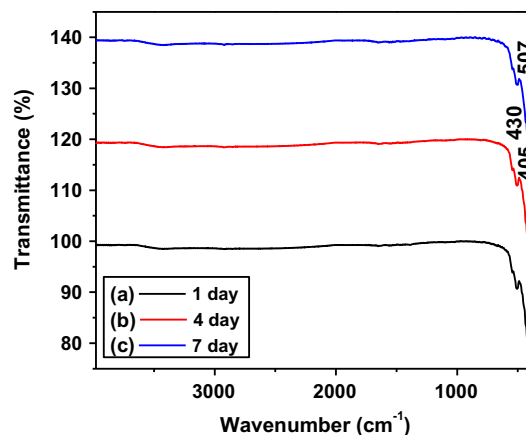


Fig. 4 IR spectra: reaction product from the mixture of 0.1 M SnCl₄ · 5H₂O and 10 ml extract (a) 1, (b) 4, (c) 7 days

bandgap energy, the obtained emission band cannot be assigned to band-edge or to exciton recombination emission. The observed clear individual emission band at 543 nm may be attributed to radiative states of the visible PL emission. It is commonly attributed to oxygen vacancies of tetragonal rutile SnO₂. A similar result was observed in XPS studies.

The FTIR spectra of 1, 4 and 7 days incubated product mixture are shown in Fig. 4a–c. The spectra were recorded in the range of 500–4,000 cm⁻¹. The absorption band observed at 405, 430 and 507 cm⁻¹ were associated with Sn–O stretching modes of vibration. The appearance of this band clearly revealed the presence of SnO₂ in the crystalline phase. No other band was observed. The obtained IR bands confirmed the formation of SnO₂ nanocrystals which can be correlated in line with the XRD results.

The composition and chemical valence state of the elements existing in SnO₂ nanocrystals was systematically characterized employing XPS as shown in Fig. 5a–l. Figure 5a–c shows the survey XPS spectra of 1, 4 and 7 days of reaction products. From survey XPS spectra (Fig. 5a–c), only Sn and O related core levels were detected which again confirmed the purity of SnO₂. The high resolution spin–orbit components (*3d*_{3/2} and *3d*_{5/2}) of the Sn*3d* peak were both observed at 496 and 487 eV as shown in Fig. 5d–f corresponding to Sn⁴⁺ in a tetragonal rutile structure [35, 36]. And the peaks corresponding to Sn²⁺ were not detected. Figure 5g–i shows the O*1s* core level spectra. The calculated composition of SnO₂ nanocrystals was given in Table 1. As the incubation and aging treatment was increased.

TEM images of the prepared nanocrystalline SnO₂ nanocrystals for different incubation and aging treatment are shown in Fig. 6a–i. The TEM images of 1 day incubated SnO₂ product clearly revealed the size

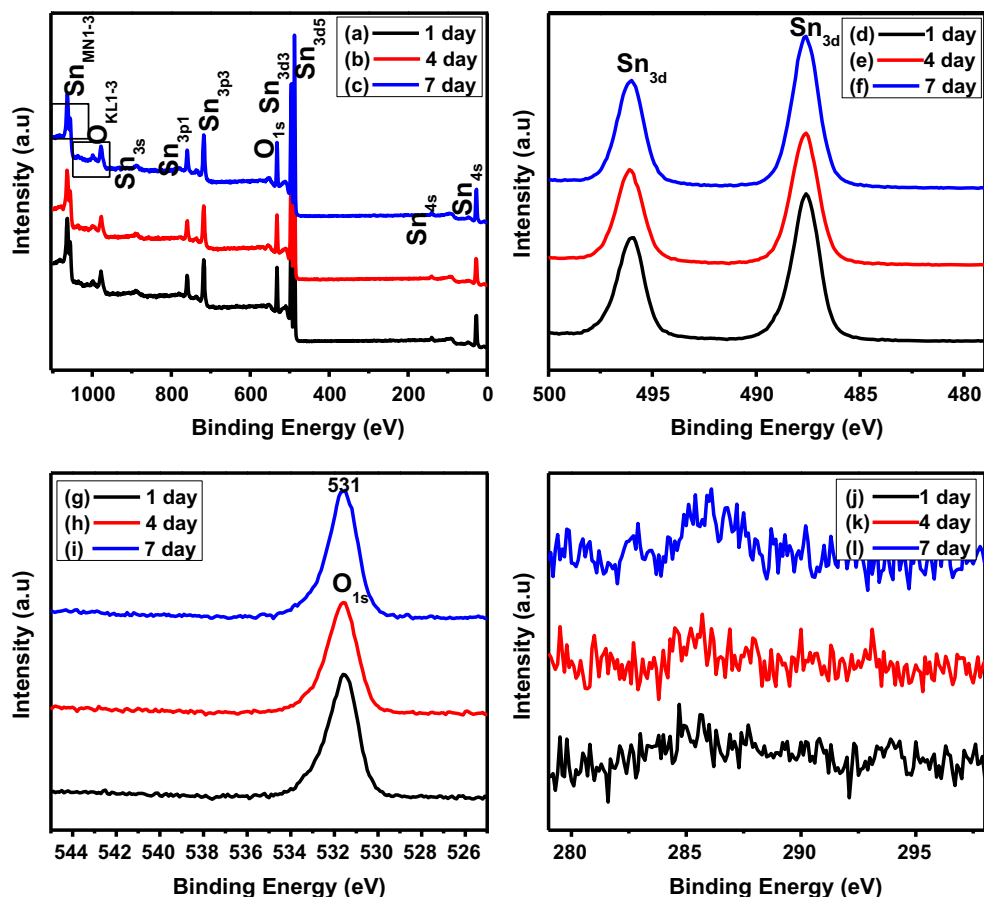


Fig. 5 XPS pattern: (a–c) Survey, (d–f) Sn_{3d}, (g–i) O_{1s}, (j–l) C_{1s} scan of 1, 4 and 7 days of reaction product from the mixture of 0.1 M SnCl₄ · 5H₂O and 10 ml extract

Table 1 XPS compositional characterization of the obtained product

Sample	Element	Start BE	Peak BE	End BE	Height CPS	FWHM (eV)	Area (P) CPS (eV)	Area (N) KE ^{0.6}	At.%
1 day	Sn _{3d}	500	487.59	482.7	56,455.44	1.51	164,721.32	2,005.86	41.44
	O _{1s}	537.2	531.55	528.1	13,464	1.6	25,149.8	2,630.14	54.33
	C _{1s}	295.4	284.83	280	131.04	0	684.04	204.84	4.23
4 day	Sn _{3d}	499.9	487.64	483.2	50,432.21	1.53	148,030.08	1,802.61	40.67
	O _{1s}	537	531.61	527.7	12,320.7	1.62	23,590.9	2,467.13	55.67
	C _{1s}	292	285.65	280.19	134.5	0.21	542.02	162.32	3.66
7 day	Sn _{3d}	499.9	487.62	483.2	58,151.88	1.49	165,677.87	2,017.51	41.08
	O _{1s}	536.5	531.57	527.8	14,155.82	1.57	26,276.84	2,748.01	55.95
	C _{1s}	291.7	285.96	280.2	144.61	0.35	487.16	145.9	2.97

ranges from 100 to 250 nm. However, the average size of 4 day incubated SnO₂ product were 175–350 nm. Moreover, the growth and shape of the nanostructures particularly depend on the incubation and aging treatments. 7 day incubated product was clearly revealed that the size of the obtained product was in the range of 200–400 nm. The selected area electron diffraction (SAED) patterns clearly

revealed the ring as well as lattice fringe formation when incubation period was increased. Three main identified planes such as (1 1 0), (1 0 1), (2 1 1) observed in SAED pattern (Fig. 6c) were in good agreement with the results obtained from XRD pattern. The size of the particle increased when incubation and aging treatment was increased. Little agglomerated particles formation was

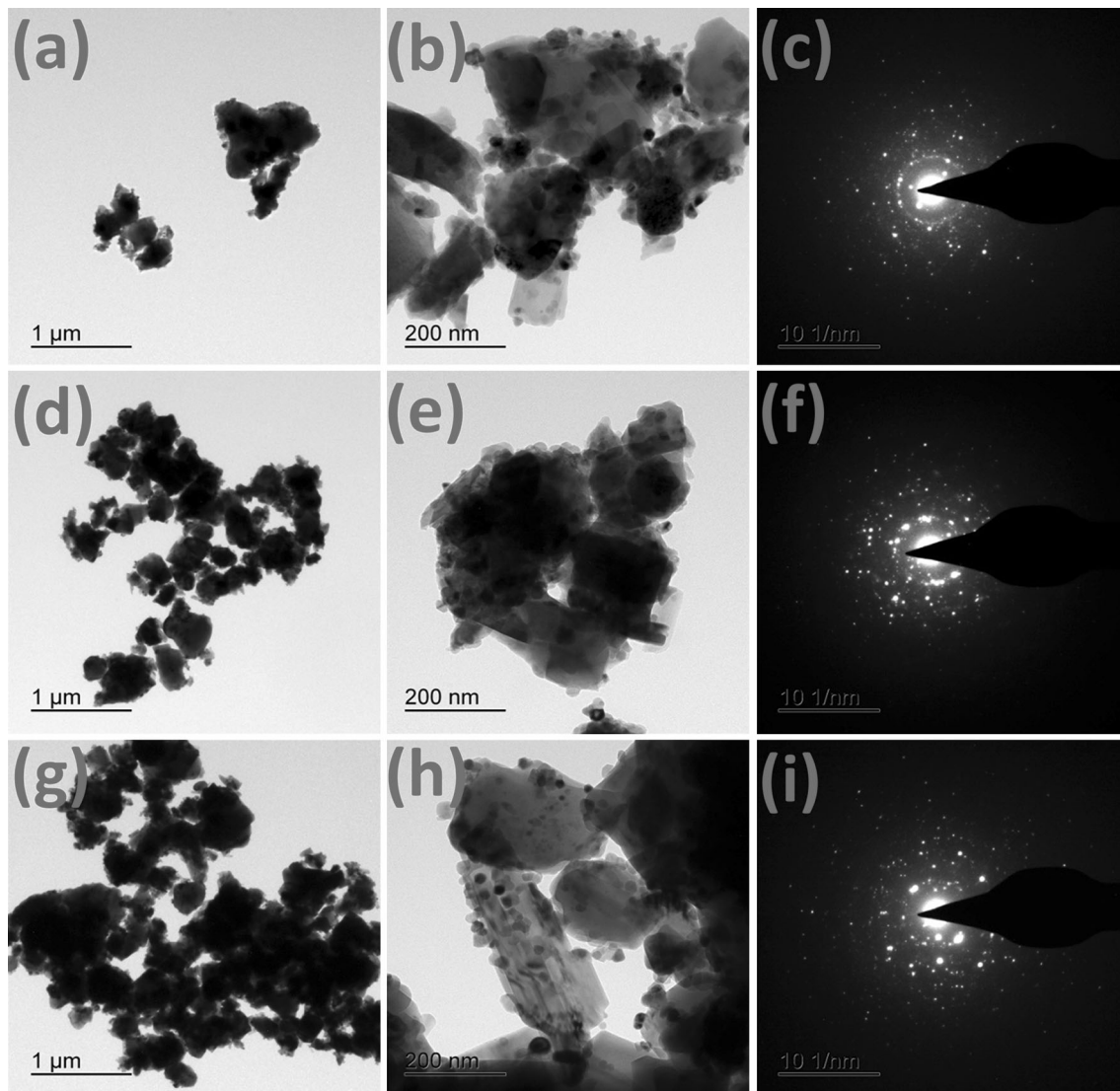


Fig. 6 TEM image: a–c 1, d–f 4, g–i 7 days of reaction product from the mixture of 0.1 M $\text{SnCl}_4 \cdot 5\text{H}_2\text{O}$ and 10 ml extract

observed at 1 day when compared to 4 and 7 days. Well isolated irregular shaped crystallites were observed at 1 day aging treatment, while more aggregated crystallites was observed at 4 and 7 days of aging treatment. The results were consistent with the crystallite size as calculated from XRD pattern. The obtained TEM micrographs clearly revealed that the grain size and agglomeration was increased at higher incubation and aging treatments.

The obtained product results in the present study have been compared with Vidhu et al. and Srivastava et al. study. Vidhu et al. [29] studied biogenic synthesis of SnO_2 nanoparticles and its evaluation of antibacterial and antioxidant activities. They emphasized an unexploited, cost effective and environmentally benign method of synthesizing bioactive tin oxide nanoparticles of size from 2.1 to 4.1 nm using *Saraca indica* flower. They further revealed

an increase in particle size was observed with increasing annealing temperature. They could attained fine tuning of band gap as evidenced in photoluminescence emission. They further explored that oxygen vacancies play an important role on PL emission. In a separate study, Srivastava et al. [30] employed biosynthesis of SnO_2 nanoparticles using bacterium *erwinia herbicola* and their photocatalytic activity for degradation of dyes. They were synthesized tetragonal SnO_2 nanoparticles (15–40 nm) employing a green biological synthesis technique using Gram-negative bacteria *Erwinia herbicola* followed by an annealing treatment over 425 K. They demonstrated that the bacterial protein and biomolecules served as the template for reduction, stabilization and controlling size and aggregation of SnO_2 nanoparticles. In the present work, SnO_2 nanocrystals were prepared employing rambutan peel

extract mediated green synthesis route without surfactant and template at room temperature incubation and aging over a period of 1, 4 and 7 days. The utilized rambutan peels has the capability of ligating SnO₂ nanocrystals [31–34]. 1, 4 and 7 days of incubation and aging treatment increased the size, crystallinity and pure phase of the obtained cassiterite type tetragonal rutile SnO₂ nanocrystals which could be useful and applied for potential industrial applications.

4 Conclusions

In summary, tetragonal rutile phase SnO₂ nanocrystal over a period of incubation was explored employing a simple and cost effective sustainable green synthesis method. The structure, morphology and compositional property of SnO₂ nanocrystal were characterized by XRD, Raman, PL, IR, XPS and TEM studies. The incubation and aging treatment affects the particle size of the synthesized samples. The obtained green synthesized pure rutile phase SnO₂ nanocrystals were showed good structural, compositional and textural properties beneficial in the development of potential industrial applications.

Acknowledgments This work was supported by a grant from the BAERI program, through the National Research Foundation of Korea (2014).

References

1. S.A. Pianaro, P.R. Bueno, P. Olivi, E. Longo, J.A. Varela, J. Mater. Sci. Mater. Electron. **9**, 159–165 (1998)
2. H. Shiomi, H. Kobayashi, T. Kimura, M. Nakamura, J. Mater. Sci. Mater. Electron. **7**, 437–445 (1996)
3. H.H. Afify, F.S. Terra, R.S. Momtaz, J. Mater. Sci. Mater. Electron. **7**, 149–153 (1996)
4. H.H. Afify, R.S. Momtaz, W.A. Badawy, S.A. Nasser, J. Mater. Sci. Mater. Electron. **2**, 40–45 (1991)
5. A.K. Hassan, R.D. Gould, A.G. Keeling, E.W. Williams, J. Mater. Sci. Mater. Electron. **5**, 310–314 (1994)
6. D.R. Acosta, A. Maldonado, R. Asomoza, J. Mater. Sci. Mater. Electron. **4**, 187–191 (1993)
7. J. Echigoya, S. Kato, H. Enoki, J. Mater. Sci. Mater. Electron. **3**, 168–171 (1992)
8. G.F. Menegotto, S.A. Pianaro, A.J. Zara, S.R.M. Antunes, A.C. Antunes, J. Mater. Sci. Mater. Electron. **13**, 253–256 (2002)
9. D. Fink, A. Kiv, V. Golovanov, J. Chen, A. Chandra, M. Ivanovskaya, L. Khirunen, D. Fuks, J. Mater. Sci. Mater. Electron. **19**, 1222–1227 (2008)
10. V. Senthilkumar, P. Vickraman, M. Jayachandran, C. Sanjeevraja, J. Mater. Sci. Mater. Electron. **21**, 343–348 (2010)
11. G. Zhou, S. Ni, X. Sun, X. Wang, Q. Wang, D. He, J. Mater. Sci. Mater. Electron. **22**, 174–178 (2011)
12. O.A. Omar, H.F. Ragaie, W.F. Fikry, J. Mater. Sci. Mater. Electron. **1**, 79–83 (1990)
13. S.G. Ansari, S.W. Gosavi, S.A. Gangal, R.N. Karekar, R.C. Aiyer, J. Mater. Sci. Mater. Electron. **8**, 23–27 (1997)
14. S.G. Ansari, P. Boroojerdian, S.K. Kulkarni, S.R. Sainkar, R.N. Karekar, R.C. Aiyer, J. Mater. Sci. Mater. Electron. **7**, 267–270 (1996)
15. Y. Liu, W. Zhu, O.K. Tan, X. Yao, Y. Shen, J. Mater. Sci. Mater. Electron. **7**, 279–282 (1996)
16. K.H. Song, S.J. Park, J. Mater. Sci. Mater. Electron. **4**, 249–253 (1993)
17. A.R. Gardeshzadeh, B. Raissi, E. Marzbanrad, H. Mohebbi, J. Mater. Sci. Mater. Electron. **20**, 127–131 (2009)
18. M. Choudhary, V.N. Mishra, R. Dwivedi, J. Mater. Sci. Mater. Electron. **24**, 2824–2832 (2013)
19. V. Agrahari, M.C. Mathpal, M. Kumar, A. Agarwal, J. Alloys Compd. **622**, 48–53 (2015)
20. A.B. Glot, R. Bulpett, A.I. Ivon, P.M. Gallegos-Acevedo, Phys. B **457**, 108–112 (2015)
21. J. Gajendiran, V. Rajendran, Mat. Lett. **139**, 116–118 (2015)
22. R. Han, H. Yang, D. Wang, X. Du, Y. Yan, J. Magn. Magn. Mater. **374**, 197–204 (2015)
23. T. Yang, J. Zhao, X. Li, X. Gao, C. Xue, Y. Wu, R. Tai, Mat. Lett. **139**, 39–41 (2015)
24. S. Xu, K. Kan, Y. Yang, C. Jiang, J. Gao, L. Jing, P. Shen, L. Li, K. Shi, J. Alloys Compd. **618**, 240–247 (2015)
25. M.V. Reddy, L.Y. Tse, W.K.Z. Bruce, B.V.R. Chowdari, Mat. Lett. **138**, 231–234 (2015)
26. T. Tao, L. He, J. Li, Y. Zhang, Mat. Lett. **138**, 45–47 (2015)
27. S.M. Andersen, C.F. Norgaard, M.J. Larsen, E. Skou, J. Power Sources **273**, 158–161 (2015)
28. L. Chen, X. Li, Y. Wang, C. Gao, H. Zhang, B. Zhao, F. Teng, J. Zhou, Z. Zhang, X. Pan, E. Xie, J. Power Sources **272**, 886–894 (2014)
29. V.K. Vidhu, D. Philip, Spectrochim. Acta Part A **134**, 372–379 (2015)
30. N. Srivastava, M. Mukhopadhyay, Ind. Eng. Chem. Res. **53**, 13971–13979 (2014)
31. R. Yuvakkumar, J. Suresh, A. Joseph Nathanael, M. Sundrarajan, S.I. Hong, Mater. Sci. Eng. C **41**, 17–27 (2014)
32. R. Yuvakkumar, J. Suresh, A. Joseph Nathanael, M. Sundrarajan, S.I. Hong, Mat. Lett. **128**, 170–174 (2014)
33. R. Yuvakkumar, J. Suresh, B. Saravanakumar, A. Joseph Nathanael, S.I. Hong, V. Rajendran, Spectrochim. Acta Part A **137**, 250–258 (2015)
34. R. Yuvakkumar, A. Joseph Nathanael, S.I. Hong, RSC Adv. **4**, 44495–44499 (2014)
35. H.J. Ahn, H.C. Choi, K.W. Park, S.B. Kim, Y.E. Sung, J. Phys. Chem. B **108**, 9815–9820 (2004)
36. K. Xu, D. Zeng, J. Wu, Q. Mao, S. Tian, S. Zhang, C. Xie, Sens. Actuators B **205**, 416–425 (2014)